FTIR Measurement of Absorption Solvents in Bioenergy Carbon Capture and Storage Processes

David Danielsen, Emma Hedberg, Isa Pettersson Haag & Oliver Svahn
Supervisor: Matthäus Bäbler
Division of Process Technology

KTH Royal Institute of Technology

KA103X, 15 hp
6 June 2023

Abstract

The effects of global warming are well understood. In order to combat this, society must move towards net zero emissions of green house gases, where carbon dioxide (CO_2) plays a key role. In several IPCC climate scenarios that meet the Paris agreement, negative emission technologies that effectively remove CO_2 from the atmosphere are included. Of several different technologies, bioenergy with carbon capture and storage (BECCS) is one of the most mature. This technology utilises an absorption-desorption process where CO_2 is solved in liquid, producing a rich solvent, and later desorbed, resulting in pure CO_2. There are, however, still challenges to implement this technology on a large scale, and one such issue is the monitoring of process streams to gain control over process conditions and system parameters.

In this project, the absorption solvent in BECCS processes were mimicked in order to determine if FTIR spectroscopy could be used to produce process parameters that are accurate, sensitive and robust. Accuracy and sensitivity are defined as the ability to correctly predict the presence and amount of species of interest in the absorption liquid. Robustness on the other hand is defined as the ability to produce precise measurements in the presence of pollutants. To evaluate how accurate and sensitive the measurements are, two different numerical models were developed and calibrated using prepared samples mimicking an absorption solvent. One model was solely based on the least square method, whereas the other was based on principal component analysis (PCA). These models were then tested on clean validation samples, as well as pilot plant samples from Stockholm Exergi, in a case study. An analysis of FTIR spectra from simulated absorption liquids showed that it could distinguish between the species of interest. Furthermore, the spectra showed that pollutants did not impact the readings in a major way. The results showed that both models produced accurate predictions of process parameters.

Sammanfattning

Effekterna av den globala uppvärmningen är välkända. För att bekämpa detta måste samhället gå mot nettonollutsläpp av växthusgaser, där koldioxid (CO_2) spelar en nyckelroll. I flera av IPCC:s klimatscenarier som uppfyller Parisavtalet ingår tekniker för negativa utsläpp, vilka för bort CO_2 från atmosfären. Av flera olika tekniker är *bioenergy with carbon capture and storage* (BECCS) en av de mest utvecklade. Denna teknologi använder en absorptions-desorptionsprocess där CO_2 absorberas i en vätska. Absorptionen ger ett så kallat rikt flöde som senare desorberas, vilket resulterar i isolationen av ren CO_2. Det finns dock fortfarande utmaningar med att implementera denna teknik i stor skala. En av dessa är övervakning av processströmmar för att få kontroll över processförhållanden och systemparametrar.

I detta projekt skapades prover som imiterade absorptionsvätskan i BECCS för att avgöra om FTIR-spektroskopi kunde användas för att ta fram exakta, känsliga och robusta processparametrar. Exakthet och känslighet definieras som förmågan att korrekt förutsäga närvaron och mängden av föreningar av intresse i absorptionsvätskan. Robusthet definieras vidare som förmågan att göra exakta mätningar i närvaro av föroreningar. För att utvärdera hur exakta och känsliga mätningarna var utvecklades och kalibrerades två olika numeriska modeller. Detta gjordes med hjälp av förberedda prover som efterliknade absorptionsvätskan. Den ena modellen baserades på minsta kvadratmetoden, medan den andra baserades på principalkomponentanalys (PCA). Dessa modeller utvärderades sedan med rena valideringsprover, samt pilotanläggningsprover från Stockholm Exergi, i en fallstudie. Resultaten från valideringsproven visade att båda modellerna kunde förutsäga processparametrar med hög precision. Utvärdering av FTIR-spektrum visade att FTIR kunde skilja mellan föreningar av intresse. Vidare visade resultaten att föroreningar inte allvarligt påverkade spektrumens karaktär.

Table of Content

1. Introduction

1.1 Background

In 2017, anthropogenic global warming reached approximately 1 ℃ above pre-industrial levels. This has led to an increasing frequency and magnitude of events such as heat waves and heavy precipitation, as well as an increased risk of drought. As concluded by IPCC (1), the accumulated emissions from human activities up until 2018 would likely not result in further warming greater than 0.5 ℃. Any overshoot of global warming of 1.5 ℃ could in part be attributed to continued anthropogenic CO_2 emissions. Climate-related risks are dependent on how high global warming reaches, where higher temperatures are associated with more severe impacts. Effects may be long-lasting or irreversible. In addition to reducing greenhouse gas emissions to zero, net negative emissions may be required. (1)

In several climate scenarios, negative emission technologies (NETs) are included in order to reach the goals set in the Paris Agreement. The term NET encompasses technologies that achieve a reduction in atmospheric CO_2 concentration. There exists several different NETs that on a theoretical level can remove CO_2 from the atmosphere. One technology that plays a key role in both reduction of emissions and in several NETs is carbon capture and storage (CCS). This is a process where CO_2 can be captured directly from flue gases for subsequent geological storage. Today, the majority of existing CCS is deployed in the oil industry. If on the other hand CCS is deployed to capture CO_2 arising from biomass incineration in bioenergy plants, it becomes a NET, known as bioenergy with carbon capture and storage (BECCS). (2)

BECCS is among the most advanced negative emission technologies. Here, negative emissions are achieved through incineration of biomass that during its lifetime has absorbed CO_2 through photosynthesis, and subsequent capture of CO_2 from the flue gas. The CO_2 is then deposited in a geological storage by injecting the captured gas into porous rock formations, commonly abandoned oil and gas fields. BECCS thus creates negative emissions, meanwhile providing fossil free energy (3). Bioenergy can be produced from several different sources, such as waste from pulp and paper mills, purposely grown biomass and biogas from wastewater treatment. In Europe, the point sources with the greatest potential for BECCS are incinerators at pulp and paper mills, contributing with emissions of 62 Mtons CO_2 annually (4). Sweden has the highest potential for negative emissions due to high biogenic CO_2 emissions. For BECCS to produce negative emissions, however, the captured amount of CO_2 must be greater than the associated greenhouse gas emissions produced throughout its lifecycle. (4)

Large point sources of greenhouse gas emissions can be retrofitted with CCS capacity using an absorption process. This is a mature technology that uses an absorption liquid to wash CO_2 from a flue gas, and is already widely used and can be readily fitted onto existing plants (5). However, early projects to develop BECCS facilities lack methods to perform real-times

in-situ analysis of process streams. Monitoring the CO_2 content in the process streams is a necessity in order to optimise process parameters. Real-time monitoring eliminates the inherent delay between sampling and analysis. In order for absorption to be a feasible technology for BECCS, this issue must be tackled. One possible method for real-time analysis is FTIR spectroscopy. Using an FTIR probe it would be possible to perform real-time and *in-situ* analysis on the solvent.

1.1.2 Purpose

The purpose of this project is to determine the feasibility of using FTIR for real-time measurements on CO_2 contents of liquid streams in BECCS processes. In order to convert FTIR data to relevant process parameters, numerical models will be developed. Three parameters will be used to evaluate the feasibility: sensitivity, robustness and accuracy. Sensitivity refers to the ability of FTIR to distinguish key components in the streams. Robustness is defined as how the measurement quality is affected by pollutants. Lastly, accuracy refers to how accurate the stream contents can be predicted.

1.2 Theory

1.2.1 BECCS

Separation of CO_2 from flue gas is conducted using an absorption-desorption process, as illustrated in *Fig. 1*. Flue gas from the biomass incineration enters the absorption column and is met with a lean solvent, the absorbent. As the flue gas gets in contact with the lean solvent, mass transfer of CO_2 occurs because of the difference in concentrations. The clean flue gas is released into the atmosphere and the absorbent leaves the absorption column as a rich solvent and enters the strippig column. In the stripping column, CO_2 is desorbed using a counter current steam, which is then condensed, resulting in a gas stream of pure CO_2. The most energy intensive part of the system in *Fig. 1* is the reboiler, and through effect optimisation the energy demand for the process can be reduced.

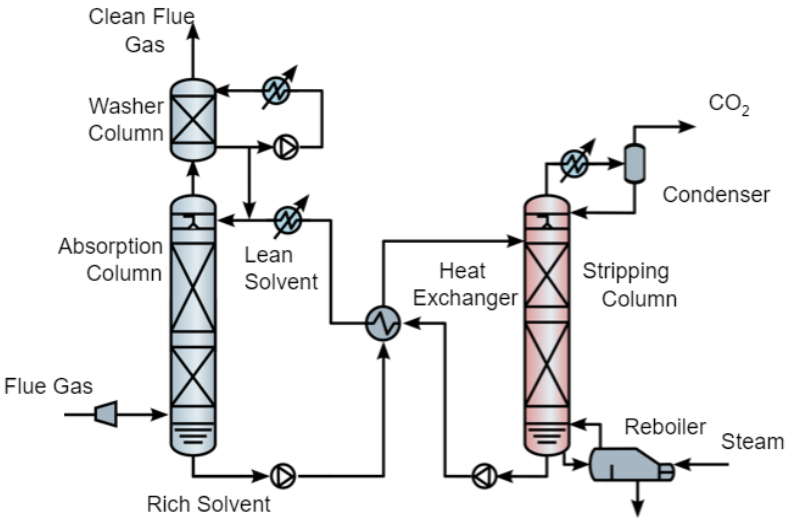

Figure 1. A schematic diagram of the absorption-desorption process.
Image courtesy of Assoc. Prof. M. Bäbler, Division of Process Technology, KTH.

The solubility of CO_2 into the liquid phase relies on the process conditions and the solvent utilised in the absorption column. Commonly used solvents for absorption of CO_2 is aqueous solutions with high pH. CO_2 forms carbonic acid when dissolved in water, which is part of an acid-base reaction. Making the aqueous solution basic, the amount of CO_2 absorbed will increase according to Le Chatelier's principle.

In this project an aqueous solution of potassium carbonate will be used to mimic the solvent utilised in BECCS process, which is often called “hot potassium process” (5). The reaction formulas below describe the absorption of CO_2 using the hot potassium carbonate process (6).

$$\mathrm{CO_3^{2-}}(aq) + \mathrm{H_2O} \rightleftharpoons \mathrm{OH^-}(aq) + \mathrm{HCO_3^-}(aq) \quad (1)$$

$$\mathrm{CO_2}(aq) + \mathrm{OH^-}(aq) \rightleftharpoons \mathrm{HCO_3^-}(aq) \quad (2)$$

Eq. 1 describes the acid-base reaction transforming carbonate (CO_3^{2-}) to bicarbonate (HCO_3^-). *Eq. 2* describes the hydrolysis of CO_2 in the alkaline K_2CO_3 solution. The dissolution of CO_2 into the solvent is slow, meaning that *Eq. 2* is the rate determining step. Therefore, rate promoters that have a catalytic effect on the reaction are used (6).

As previously mentioned, FTIR could be utilised for real-time solvent analysis. It is a commonly used spectroscopy method for identification and characterisation of functional groups in organic and inorganic materials. When infrared radiation passes through a sample it can be absorbed by molecules, exciting molecular bonds to higher vibrational energy at specific wavelengths. As the excitation occurs at quantified and specific wavenumbers, the method can distinguish between different molecular bonds. The method is non-destructive and can be used for real-times analysis *in-situ* (7).

1.2.2 Solvent strength and solvent loading

When dissolving CO_2 into an aqueous solution containing K_2CO_3, the net reaction from *Eq. 1* and *2* occurs according to *Eq. 3*.

$$K_2CO_3 + CO_2 + H_2O \rightleftharpoons 2\ KHCO_3 \tag{3}$$

Hence, the hot-potassium solvent can be seen as an aqueous mixture of K_2CO_3 and $KHCO_3$. The more CO_2 the solvent has taken up, the higher the concentration of $KHCO_3$ and the lower the concentration of K_2CO_3. The absorbent is often described using two parameters, the solvent strength, *X*, and the solvent loading, θ. The solvent strength is defined as the weight percentage of K_2CO_3 equivalents in the native solvent, i.e a solution solely containing K_2CO_3 and water, whilst solvent loading is defined as the ratio between the moles of CO_2 absorbed by the solvent and K_2CO_3 equivalents in the native solution. Solvent strength and solvent loading are described in *Eq. 4.1* and *4.2* respectively.

$$X = wt\%\ K_2CO_3\ equiv. \tag{4.1}$$

$$\theta = \frac{(moles\ CO2\ absorbed)}{(moles\ K2CO3\ equiv.)} \tag{4.2}$$

Further on, the solvent loading and solvent strength can be expressed through the weight fraction of K_2CO_3 and $KHCO_3$ according to *Eq. 5.1-5.2*. To determine error propagation when calculating X and θ using *Eq. 5.1-5.2*, *Eq. 5.3* was used.

$$X = \frac{2w_1M_2+w_2M_1}{2(1-w_2)M_2+w_2(M_1+M_3)} \tag{5.1}$$

$$\theta = \frac{w_2}{2(M_2/M_1)w_1+w_2} \tag{5.2}$$

$$e_f = \left|\frac{\partial f}{\partial w_1}\right| e_{w1} + \left|\frac{\partial f}{\partial w_2}\right| e_{w2} \tag{5.3}$$

In *Eq. 5.1-5.2,* w_1 is the weight fraction of K_2CO_3 and w_2 is the weight fraction of $KHCO_3$. Additionally, M_1, M_2, and M_3 are the molar mass of K_2CO_3, $KHCO_3$, and H_2O respectively.
In *Eq. 5.3, f* is a placeholder for X or θ and e_i represent the error for variable *i*. Derivation of *Eq. 5.1-5.2* is available in Attachment 1.

With FTIR data as input in numerical models, weight fractions of K_2CO_3 and $KHCO_3$ can be estimated. However, the parameters of interest on a process-level are solvent strength and solvent loading, which may be calculated from weight fractions according to *Eq. 5.1* and *5.2*. The equations describe the transformation of points in the weight fraction plane to the *X*-θ plane as shown in *Fig. 2*. A rearrangement of the equations yields transformations that maps points in the *X*-θ plane onto the weight fraction plane.

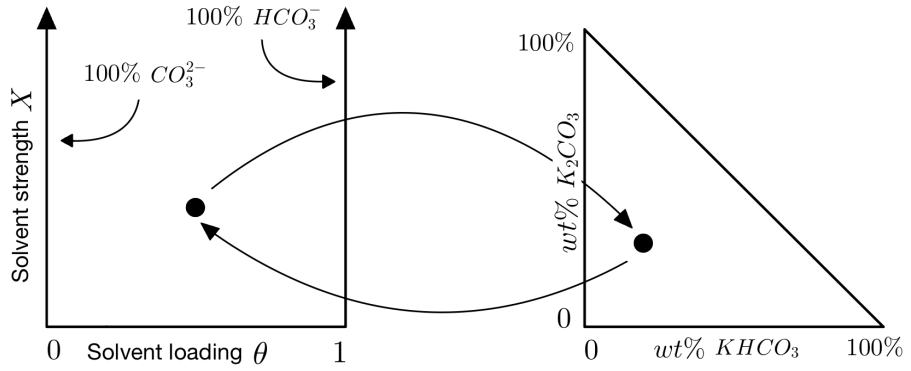

Figure 2. An illustration of a single sample with solvent loading, θ, and solvent strength, X converted into weight fraction of CO_3 and HCO_3 using equations 5.1-5.2.

In figure 2, the left plot is the X-θ plane and the right plot is the weight fraction plane. In the X-θ plane the solvent loading varies from zero to one. A loading of zero corresponds to a pure carbonate solution, whereas a loading of one corresponds to a solution of pure bicarbonate.

1.2.3 PCA

Section 1.2.3 is exclusively based on chapter four of the book Multivariate Data Analysis (8). Care has been taken to not copy the text *verbatim*, though there is much resemblance between this content and that of the book.

When creating a model from a set of measurements, some systematic variance within the data is commonly what we are interested in. In most cases, measurements are carried out several times and each time, a certain number of variables are measured. For all cases where more than one variable is measured, the action of analysing the data becomes a multivariate analysis problem. The method chosen in this project is principal component analysis (PCA), which both reduces the dimensionality of the data and finds the most significant variance within the set.

Consider a data set of n measurements, called objects, for which p variables have been measured. This data may be structured in a matrix $\mathbf{X}$ of dimensions $n \times p$ so that each row represents an individual object and each column corresponds to a single variable. The objects may then be presented as scattered points in a p-dimensional coordinate system where the mutually orthogonal coordinate axes represent the variables (assuming they are independent of each other). This is called a variable space and the objects would be plotted by using the measured data from each row as coordinates. For the cases where p equals one, two or three, it is possible to visualise the scattered data points using this approach.

When measuring for example three variables x, y and z, the resulting objects can be plotted in a three-dimensional variable space. The systematic variance of interest might then manifest

itself as the points adhere to some trend, often not parallel to any of the coordinate axes. For example, they might follow a linear trend, in which case the data points could be approximated using a linear regression as illustrated in *Fig. 3*. Although the objects reside in a three-dimensional variable space, they may be effectively represented in one dimension by projection onto this line. A representation of the data using their projection "footprints" on the line is an approximation, as the projection distances are lost, but will suffice in many cases.

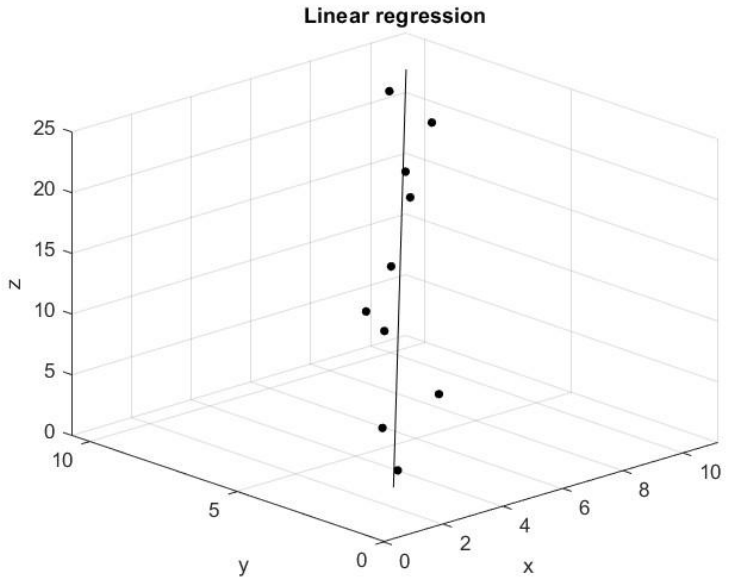

Figure 3. An illustration of a linear regression of an arbitrary data swarm in the xyz-variable space.

Fig. 3 illustrates an arbitrary data swarm in a three-dimensional variable space with an appurtenant linear regression. Notably, the line is oriented such that the distance between the objects and the line is minimised. Another way of expressing this is that the line is oriented along the direction of maximum variance in the object swarm; that which we wish to model. Hence, this approach has both reduced the dimensionality of the data from three to one dimensions and has found the most significant variance; the same objectives that PCA promises to achieve.

In PCA, the data in the matrix **X** is used as a starting input. Here, the variable space might be of an order p much higher than three so that it is impossible to visualise. From the object swarm in the variable space, principal components (PCs) are calculated and used as base vectors for a subspace akin to the one-dimensional subspace of the linear regression. The PCs are determined such that the first PC (PC_1) is parallel to the direction of maximum variance and is thus also parallel to the linear regression from *Fig. 3*. The next PC (PC_2) is then determined such that it is parallel to the direction of the second largest variance while being orthogonal to PC_1. This algorithm is then carried out for the following PCs, resulting in a set of mutually orthogonal PCs that are oriented along directions of diminishing variance. The maximum number of PCs is determined as the lesser value of either p or n-1 for the original matrix **X** and is often labelled A. A PC subspace can then be defined by the PCs centred at the

mean object, or the middle of the data swarm. As there are never more than p PCs, the subspace cannot transcend the dimensionality of the variable space.

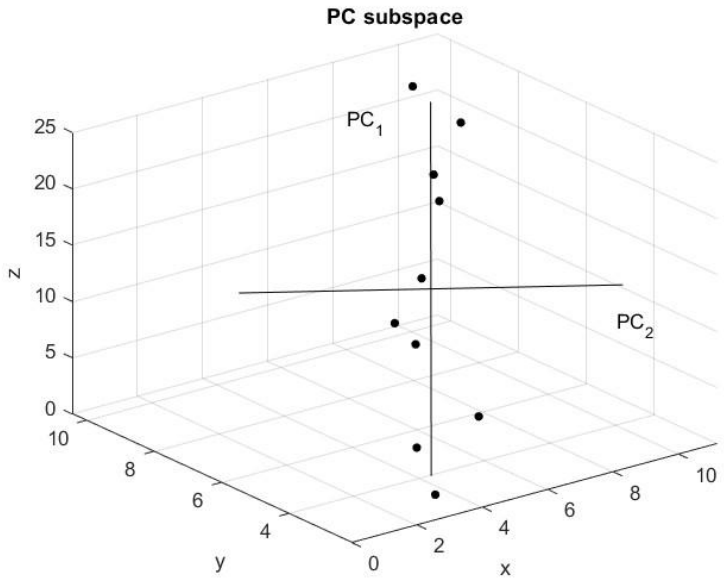

Figure 4. Illustration of PC_1 and PC_2 for an arbitrary data swarm in the xyz-variable space.

In *Fig. 4* the same arbitrary data swarm as in *Fig. 3* is portrayed in a three-dimensional variable space, along with the directions defined by PC_1 and PC_2. As the PCs are simply vectors residing in the variable space, they may be written as unique linear combinations of the variables that define the variable space. In *Eq. 6.1*, a general form of such a representation is described for a set of p variables x_i and the corresponding weighting factors p_{ij}, called loadings.

$$PC_j = p_{1j}x_1 + p_{2j}x_2 + \ \ldots \ + p_{pj}x_p \tag{6.1}$$

The loadings can be interpreted as a description of how closely related a PC is to a given variable. If the linear combination for a PC has a high loading for a variable, the orientation of the PC is closer to that of the variable. This indicates that the variable in question is responsible for a considerable amount of the variance that the PC is aligned with. Considering the PC as the result of a sum of vectors of different lengths, it becomes apparent that a vector of greater length will have a larger contribution to the direction of the resultant vector. In PCA, it is common to clump these loadings together in a loading matrix **P** defined in *Eq. 6.2*.

$$\mathrm{P} = \begin{bmatrix} p_{1,1} & \cdots & p_{1,A} \\ \vdots & \ddots & \vdots \\ p_{p,1} & \cdots & p_{p,A} \end{bmatrix} \tag{6.2}$$

The original data from **X** can be mapped in the PC space by projection of the objects onto the PCs and taking the distance from the mean object, being the origin of the PC space, to the projection footprints as coordinates. In practice, the matrix **P** is a transformation matrix for this mapping, giving rise to a central equation in PCA as described in *Eq. 7.1*.

$$\mathbf{T} = \mathbf{XP} \tag{7.1}$$

$$\mathbf{X} = \mathbf{TP^T} + \mathbf{E} \tag{7.2}$$

In *Eq. 7.1*, the **T** matrix contains the coordinates for the objects in the PC subspace, which are called scores; it is an analogy to **X** for the PC space. For a **P** matrix where $A = p$, so that **P** and **X** are equal in size, no dimensionality is lost, and the transformation consists of simply rotating and shifting the coordinate system in space. In such cases, *Eq. 7.1* holds true and **X** can be accurately described using only **T** and **P**. However, a central idea in PCA is that not all the variance in **X** is significant, only a portion of it is the result of the systematic variance we wish to model. The rest is ascribed to random errors, or noise in the measurements.

When creating a PCA based model, it is therefore desirable to separate the "structure variance" from the "noise variance". To achieve this, the number of PCs that are included in **P** is limited to less than the maximum A. The result is that the PC subspace will have a dimensionality less than that of the variable space. The mapping of data points will consequently be a projection onto this subspace, leading to a loss of information much like the case of the linear regression in *Fig. 3*. Thus, to completely describe **X** using **T** and **P**, an error matrix E must be included as described in *Eq. 7.2*, whose elements contain information on the projection distances. The E matrix is thus a measure of how well the PCA model fits the original data and a common way to account for the errors in **E** is to calculate the squared object residual, described for an object i in *Eq. 8.1.* These may then be used to calculate the total squared object residual according to *Eq. 8.2.*

$$e_i^2 = \sum_{k=1}^{p} e_{ik}^2 \tag{8.1}$$

$$e_{tot}^2 = \sum_{i=1}^{n} e_i^2 \tag{8.2}$$

The total squared object residual is a measure of how much variance the error matrix **E** describes. It also plays an important role in determining the number of PCs to include in the **P** matrix. Using *Eq. 7.2*, the matrix **P** may be constructed from the bottom up by including one PC at the time. Initially, if no PCs are included, then the product $\mathbf{TP^T}$ is zero and **X** simply equals $\mathbf{E_0}$, where the subscript 0 indicates that no PCs have been included in **P**. This means that all variance in **X** is included in $\mathbf{E_0}$ and the total squared object residual for $\mathbf{E_0}$ is at its maximum. As one PC is calculated and included in **P**, the product $\mathbf{TP^T}$ becomes non-zero and for the equality in *Eq. 7.2* to hold, the new error matrix $\mathbf{E_1}$ cannot be equal to $\mathbf{E_0}$. As the product $\mathbf{TP^T}$ models a certain part of the variance in **X**, the variance in $\mathbf{E_1}$ must be less than

that in $\mathbf{E_0}$ and consequently the new total squared object residual will be smaller than its predecessor. If this process is repeated until **P** contains *A* PCs, all variance in **X** will be modelled by the product $\mathbf{TP^T}$, as previously discussed, and $\mathbf{E}_A$ will be zero. If the total squared object residuals from each step described above is plotted against the number of included PCs in **P**, the amount of variance explained by the $\mathbf{TP^T}$ product, or the variance included in $\mathbf{E_i}$, can be visualised. This plot is called a residual calibration variance plot and commonly takes the shape of an exponential decreasing function. Most importantly, there is usually a distinct change in the angle of the plot, which provides a good starting point for determining how many PCs to include. As the PCs go from modelling systematic variance to random variance, the effect of adding another PC to **P** has a much smaller effect on the total squared object residual, as the variance is simply smaller. Although this is a useful indicator, it is still up to the data analyst to choose how many PCs the model should include. There may be reasons to include a higher or lower number of PCs than the residual calibration variance plot suggests, for example the accuracy of the measurement equipment.

2. Method

This section describes how samples were created and analysed using FTIR in order to train and validate two numerical models.

2.1 Experimental Procedure

2.1.1 Equipment and materials

Materials used was potassium carbonate [K_2CO_3, CAS: 584-08-7, Sigma-Aldrich, purity ≥ 99.0%], potassium bicarbonate [$KHCO_3$, CAS:298-14-6, Sigma-Aldrich, purity: 99.7%], ammonium chloride [NH_4Cl, CAS: 12125-02-9, Sigma-Aldrich, purity ≥ 99.5%] and vanadium pentoxide [V_2O_5, CAS: 1314-62-1, Sigma-Aldrich, Purity ≥ 99.6%]. FTIR equipment used was PerkinElmer's *Spectrum Two FT-IR Spectrometer*.

2.1.2 Training set

The experimental procedure was divided into two parts, the preparations of the samples and the analysis of the samples using the FTIR spectrometer.

The training set consisted of 24 individual samples, S1-S24, with varying solvent loading and solvent strength. The samples contained a mixture of K_2CO_3 and $KHCO_3$. Prior to preparing the samples, the solvent loading and strength were chosen strategically and the weight fraction of K_2CO_3 and $KHCO_3$ were calculated using *Eq. 5.1-5.2* for all 24 samples. The samples were then prepared in separate containers using a scale to measure up the correct amount of K_2CO_3 and $KHCO_3$. Deionized water was then weighed and added, acquiring the

desired concentration. See table A.1 in Appendix for calculated weight fractions, solvent loading and solvent strength.
After preparation, each of the 24 samples were analysed using FTIR spectroscopy. First, an air background was made, and then the sample spectra were collected. Lastly, the data for each sample was obtained and later applied to MATLAB.

2.1.3 Validation samples

Four validation samples were prepared using the same procedure as for the training set. All validation samples contained a combination of K_2CO_3 and $KHCO_3$. For information regarding weight fractions, solvent strength and loading, see *Tab. A.2* in Appendix. Furthermore, 10 additional validation samples were received from the BECCS pilot plant located at Stockholm Exergi's KVV8 facility (see *Tab. A.2* in Appendix). All validation samples were analysed using FTIR. Stockholm Exergi samples were also analysed with titration.

2.1.4 Polluted samples

An aqueous sample with a weight fraction of 0.1619 of K_2CO_3 was prepared in a container. A gas bubbler was filled with the solution and connected to vacuum on one side and a cigarette on the other. When the vacuum was turned on, the cigarette smoke bubbled through the carbonated solution. Five cigarettes were used in total whereas the filter had been removed from four of them. Additional six samples containing vanadium pentoxide and varying contents of K_2CO_3 and $KHCO_3$ were prepared (see *Tab. A.4*) and lastly, a polluted sample was prepared with weight fractions of 0.1500 K_2CO_3, 0.1002 $KHCO_3$ and 0.0508 NH_4Cl. All polluted samples were analysed using FTIR. (Filtered)

2.2 Numerical models

In the following section, two numerical models were created using all 24 samples from the training set.

2.2.1 Model 1

Given a species that absorbs radiation at wavenumbers in the IR region, a linear correlation between absorbance at a given wavenumber and concentration was assumed, in accordance with Lambert-Beers law. For the case of K_2CO_3 and $KHCO_3$, the transmittance at several wavenumbers were taken into account. The weight fractions of these species (proportional to the concentrations) in a solution are expressed by two distinct linear functions of measured transmittance at *m* wavenumbers. *Eq. 9.1-9.2* expresses this in a general form.

$$Wt_{K2CO3} = \beta_0 + \beta_1 a_{v1} + \beta_2 a_{v2} + \ \ldots \ + \beta_m a_{vm} \tag{9.1}$$

$$Wt_{KHCO3} = \gamma_0 + \gamma_1 a_{v1} + \gamma_2 a_{v2} + \ \ldots \ + \gamma_m a_{vm} \tag{9.2}$$

In the equations above, Wt_{K2CO3} and Wt_{KHCO3} are the weight fractions of K_2CO_3 and $KHCO_3$ respectively, and a_{vi} is the transmittance at wavenumber v_i. Using the training set of n samples, the least square method (LSM) was performed on *Eq. 9.3-9.4* to find the coefficient vectors β and γ. Written in a vector notation, the equation system used for LSM reads as follows:

$$\begin{bmatrix} 1 & a_{1,v1} & a_{1,v2} & \ldots & a_{1,vm} \\ 1 & a_{2,v1} & \ddots & & \vdots \\ \vdots & \vdots & & \ddots & \vdots \\ 1 & a_{n,v1} & \ldots & \ldots & a_{n,vm} \end{bmatrix} \begin{bmatrix} \beta_0 \\ \beta_1 \\ \vdots \\ \beta_m \end{bmatrix} = \begin{bmatrix} Wt_1\, K_2CO_3 \\ Wt_2\, K_2CO_3 \\ \vdots \\ Wt_n\, K_2CO_3 \end{bmatrix} \tag{9.3}$$

$$\begin{bmatrix} 1 & a_{1,v1} & a_{1,v2} & \ldots & a_{1,vm} \\ 1 & a_{2,v1} & \ddots & & \vdots \\ \vdots & \vdots & & \ddots & \vdots \\ 1 & a_{n,v1} & \ldots & \ldots & a_{n,vm} \end{bmatrix} \begin{bmatrix} \gamma_0 \\ \gamma_1 \\ \vdots \\ \gamma_m \end{bmatrix} = \begin{bmatrix} Wt_1\, KHCO_3 \\ Wt_2\, KHCO_3 \\ \vdots \\ Wt_n\, KHCO_3 \end{bmatrix} \tag{9.4}$$

The right hand side of *Eq. 9.3-9.4* are vectors representing weight fractions of K_2CO_3 and $KHCO_3$ respectively for each of the n samples. On the left hand side, the matrix with measured transmittance at the m wavenumbers for all n samples are multiplied with vectors containing the regression coefficients β_i and γ_i. In this case, $n = 24$ training set samples were used.

2.2.2 Model 2

As in model 1, a linear correlation between absorbance and the concentrations of K_2CO_3 and $KHCO_3$ was assumed. However, instead of manually picking out discrete wavenumbers from the spectrum, PCA was carried out on the entire set of training samples. From the resulting residual calibration variance plot, the number of PCs to include in the model was determined. Letting the selected PCs define the **P** matrix, the objects scores were calculated using *Eq. 7.1*. LSM was then performed on the calculated scores, yielding the regression coefficients described in *Eq. 9.1* and *9.2*. Instead of using transmittance at selected wavenumbers as variables, the regressions in model 2 uses a sample's corresponding scores, that may be calculated using *Eq. 7.1*.

3. Results and discussion

3.1 Analysis of FTIR spectra

3.1.1 Training set

In the following section, interpretations of four different spectra are to be made. The spectra were taken on the training set samples and all of the samples were analysed with an air background.

In the absorbance liquid, there is presence of both K_2CO_3 and $KHCO_3$ in the rich solvent stream from the absorption column. Therefore, *Fig. 5* was created to investigate whether K_2CO_3, $KHCO_3$, and water could be distinguished from each other in an FTIR spectrum.

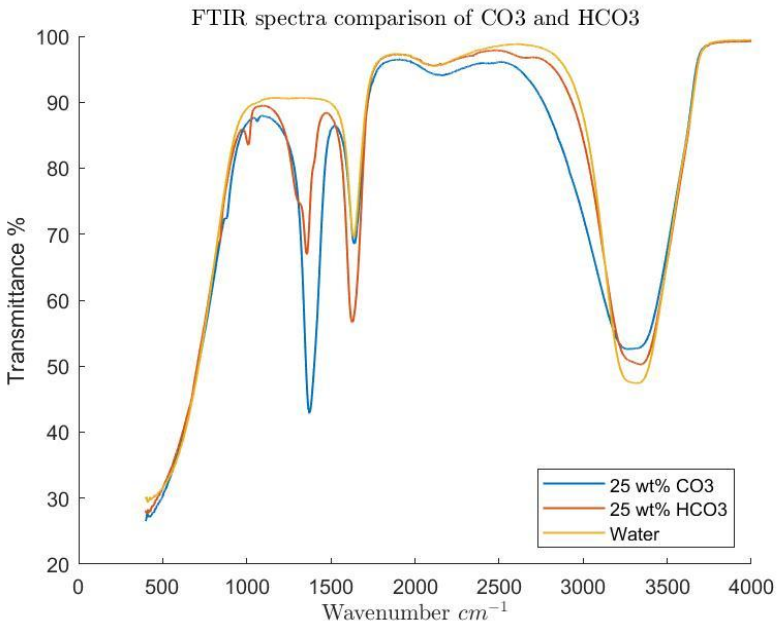

Figure 5. FTIR spectra of pure carbonate sample, pure bicarbonate sample and a water sample.

When studying *Fig. 5* it can be noted that all of the three samples display peaks within the same wavenumber intervals. However, they appear to have different peak characteristics and transmittance differences. Due to this, it is possible to visually distinguish the two substances, and with aid of *Tab. A.4* (see in Appendix) it is possible to determine each vibrational state of the molecules.

Interpreting the spectra for K_2CO_3, the blue line in *Fig. 5*, the peak maximas are approximately at wavenumbers: 1372 ; 1637 ; 3327 cm^{-1}. For $KHCO_3$ on the other hand, the peak's maximum are at 1005; 1327 ; 1627 ; 3318 cm^{-1}. Comparing the peaks to the left, at 1372 cm^{-1} for K_2CO_3 and 1327 cm^{-1} for $KHCO_3$, the peak characteristics and transmittance level differs. Based on *Tab. A.4* (see Appendix), for carbonate it is concluded to be the

vibrational state of C-O, which has an asymmetric stretching, whilst for bicarbonate it is the C-O symmetrical stretching. As observed in *Fig. 5*, there appears to be a shoulder at the left slope of the $KHCO_3$ peak at 1327 cm^{-1} (lower shoulder). This lower shoulder might be attributable to presence of CO_3^{2-} (9). Observing the spectra for bicarbonate, it has a small peak at wavenumber 1005 cm^{-1} which corresponds to an asymmetric stretching of the C-OH unit in $KHCO_3$.

Moreover, the peaks around 1600 cm^{-1} seem to have similar characteristics for all of the three samples. The only difference that stands out is the bicarbonate sample which has a lower transmittance factor compared to the other two. Rather, the carbonate and water sample appear to create the same curve, and consulting *Tab. A.4* it is concluded to be the bending mode of the water molecules. As for bicarbonate, the peak is more pronounced due to the contribution of the C-O asymmetric stretching mode in $KHCO_3$. Lastly, for the broad peaks around 3400 cm^{-1}, it is noted that all of the samples show similar trends. The peak corresponds to both symmetric and asymmetric stretching of the water molecules (10).

As previously mentioned, the absorption liquid operates at loadings between 0 and 1, meaning there is both K_2CO_3 and $KHCO_3$ present. To determine if FTIR could distinguish between mixed samples, a spectra with samples at solvent loadings 0.2 and 0.6 was created (*Fig. 6*).

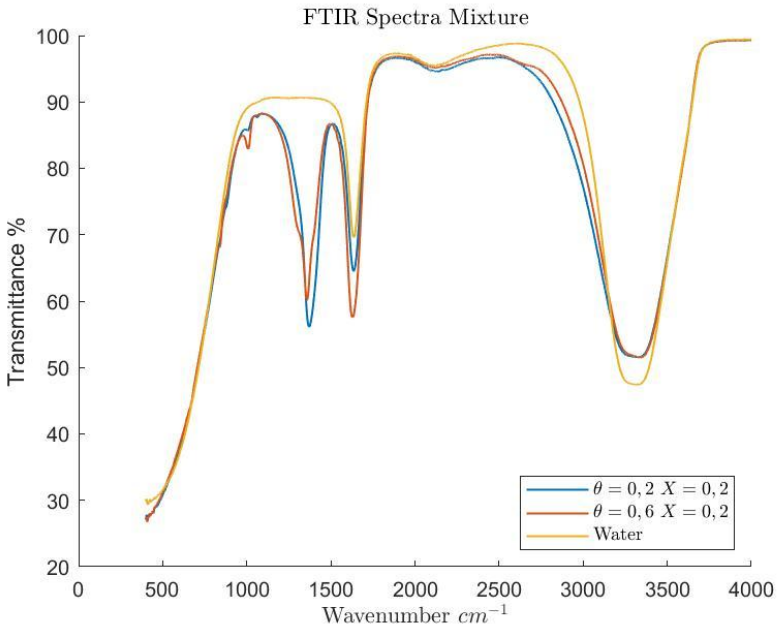

Figure. 6. FTIR spectra of mixture samples with different solvent loadings.

The components display lower transmittance around the same wavenumber intervals. Following the orange curve in *Fig. 6*, corresponding to θ = 0.6, it is noted that it has a lower shoulder, which is a typical characteristic for samples with high concentration of $KHCO_3$. It can also be noted that the blue curve, corresponding to θ = 0.2, has a lower transmittance around 1300 and a higher transmittance around 1600 cm^{-1} compared to the orange curve. By

definition, a higher ratio of $KHCO_3$ to K_2CO_3 gives a higher solvent loading. As such, the spectra in *Fig. 6* display similar trends as the spectra in *Fig. 5*, with respect to how K_2CO_3 and $KHCO_3$ influence the relative transmittance.

Another aspect that was studied was the transmittance variance due to different concentrations of a single species. *Fig. 7* illustrates one set of spectra for each component (K_2CO_3 and $KHCO_3$) with varying concentrations and constant solvent loading 0 and 1 respectively.

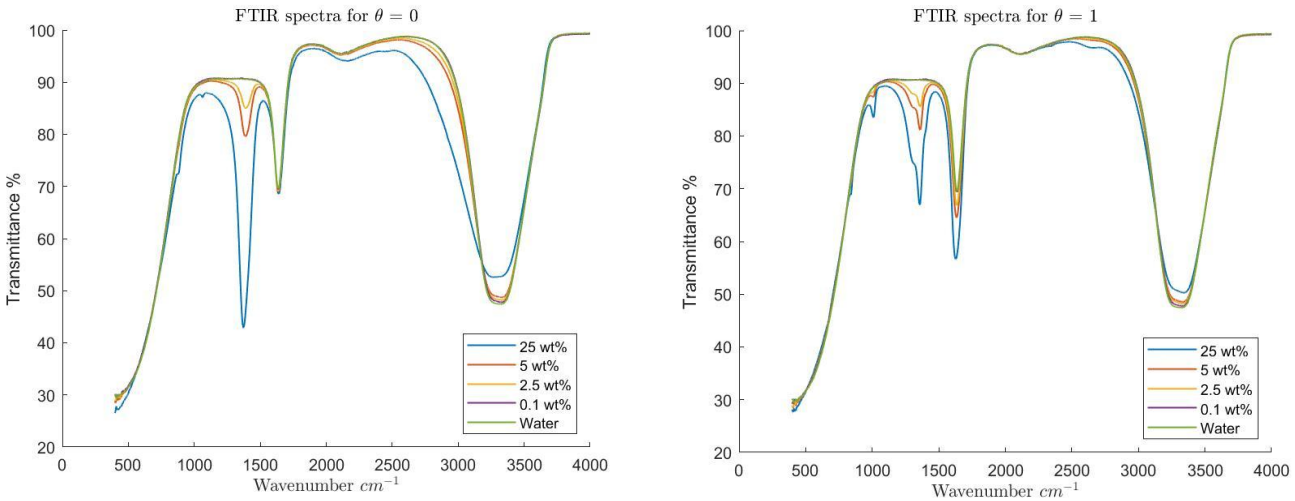

a) *b)*

Figure. 7. Two FTIR spectra illustrating four samples each with different loadings, θ, and weight percentages. (a) Spectra of pure K_2CO_3, loading zero. (b) Spectra of pure $KHCO_3$, loading one.

In both figures it can be noted that the absorbance increases for the higher weight fractions. This illustrates that there is a correlation between weight fraction of absorbing species and transmittance, giving weight to the assumption made in model 1 and 2.

In conclusion, mixtures of K_2CO_3 and $KHCO_3$ can be distinguished from each other when studying the spectra. This makes it possible to interpret whether they exist in high or in low concentrations. Furthermore, K_2CO_3 and $KHCO_3$ display unique trends in the spectra, both isolated in separate solutions and when combined. Consequently, FTIR spectroscopy can distinguish between samples with differing solvent loadings.

3.1.2 Polluted Samples

The reason for analysing polluted samples was to determine if the contaminants will disrupt the most prominent characteristics of the samples. It is very likely that the solvent in an actual absorption plant will gradually accumulate pollutants that enter the unit from the flue gas. *Fig. 8a)* shows two polluted samples, one with smoke gas and the other with ammonium (NH_4Cl). In *Fig. 8b)* three vanadium pentoxide (V_2O_5) samples are shown.

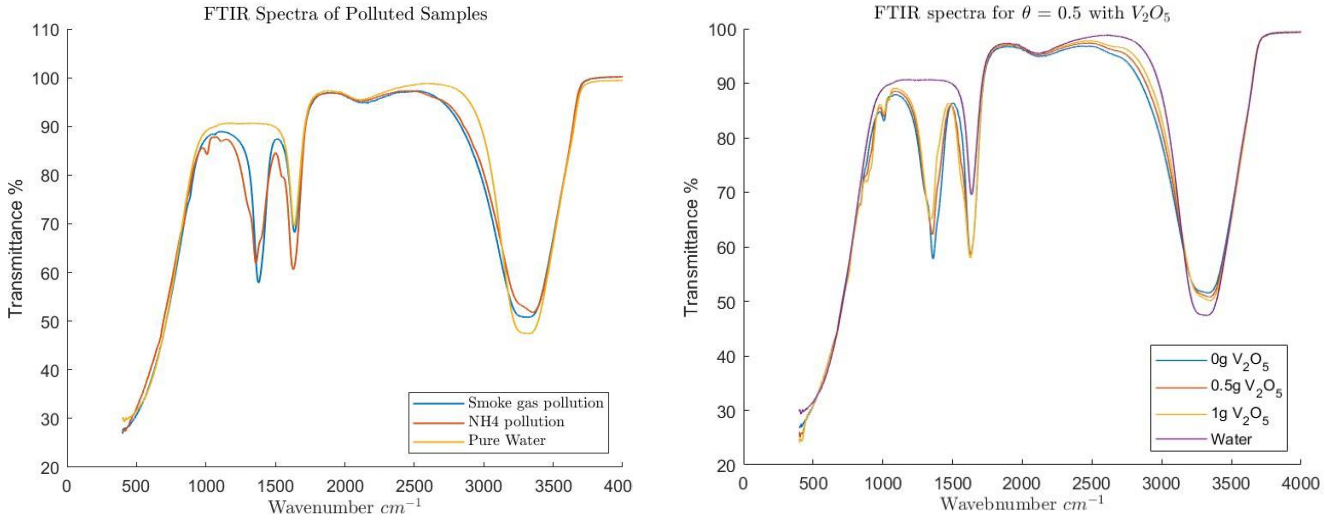

a) *b)*

Figure 8. a) FTIR spectra of polluted samples and b) samples containing the rate promoter V_2O_5.

The polluted smoke gas sample contained a mixture of K_2CO_3 and $KHCO_3$. In *Fig. 8a)* it can be observed that this polluted sample does not show significant deviations from expected characteristics. The smoke gas sample that was created by bubbling cigarette smoke through the solvent showed some visible turbidity, however, this turbidity seems not to affect the IR transmittance. This indicates that the pollution does not affect the FTIR data from the sample. However, this is not the case for the ammonia polluted sample in *Fig. 8a).* It is noted at wavenumber 1359 cm^{-1} that the peak has two lower shoulders. Previously, samples containing $KHCO_3$ showed one lower shoulder, but due to presence of ammonia it creates two. Obtaining data from FTIR with a presence of ammonia could therefore cause some skewing to the model results.

The samples displayed in *Fig. 8b)* illustrate the influence of the rate promoter V_2O_5 on the FTIR measurements. The three samples all had a solvent loading of 0.5 and solvent strength of approximately 0.21. Deviations between the spectra should then be attributable to V_2O_5, although slight variations in solvent strengths explains the transmittance differences at 1300 cm^{-1}. At the peaks around 1300 cm^{-1} and on the slopes around 1000 cm^{-1}, there seem to be slight deviations between the spectra. However, no significant differences can be observed and the expected peak characteristics are still well defined indicating that inclusion of V_2O_5 as a rate promoter does not interfere with FTIR measurements.

3.2 Model results

3.2.1 PCA metrics

Inspection of the FTIR spectra revealed that the most interesting phenomena pertaining to K_2CO_3 and $KHCO_3$ occurs in the interval 1000 to 1800 cm^{-1}. As such, the decision was made

to limit the sample data to transmittance within this interval. Upon performing PCA on the delimited training data set, a residual calibration variance plot was created to help determine how many PCs should be included in Model 2 (*Fig. 9*).

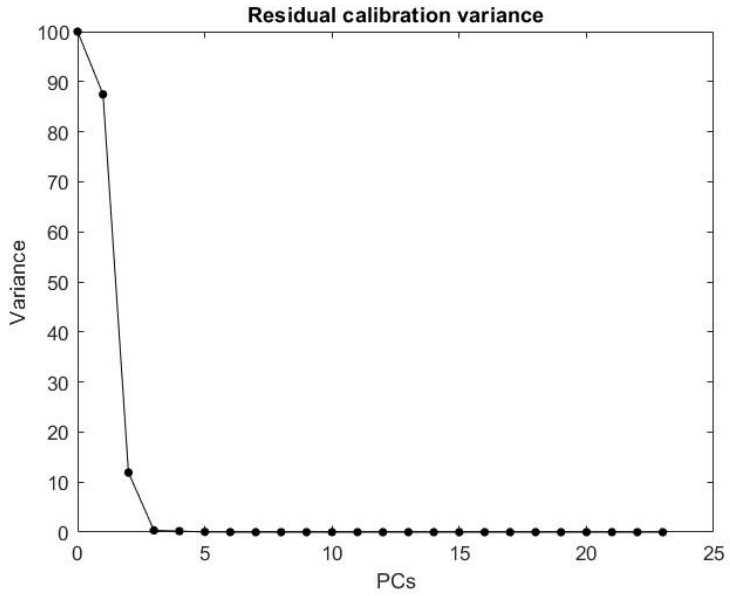

Figure 9. A residual calibration variance plot from the PCA performed on the training data set.

In *Fig. 9*, there is a clear break in the graph at PC_3, showing that PCs of higher order models have significantly less variance. This is a clear indication that PC_4-PC_{23} model variance that is the result of noise in the measurements. Consequently, it was determined that model 2 should only include the first three PCs, namely PC_1-PC_3. Having determined that the **P**-matrix should be made up of PC_1-PC_3, the squared object residuals were calculated from the E-matrix according to *Eq. 2.2*. These are presented in *Fig. 10*.

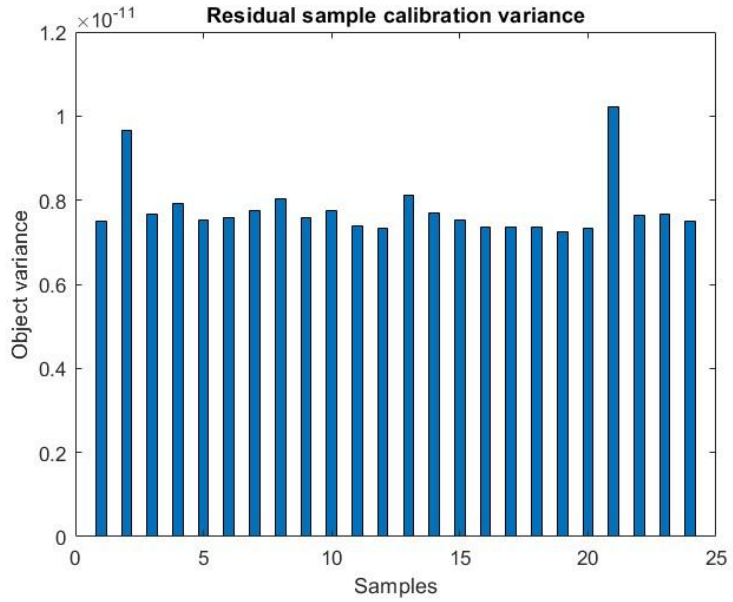

*Figure 10. A bar chart of squared object residuals for the **P**-subspace for model 2.*

Fig. 10 shows that the squared object residuals are of approximately the same size, apart from S2 and S21. However, the scale on the y-axis is in the order of 10^{-11}, meaning that the deviances of S2 and S21 from the other samples are negligible. Hence, none of the training set samples were deemed to be outliers, all 24 were included in the models.

Lastly, a loadings plot was generated for PC_1-PC_3 and is shown in *Fig. 11*, to examine where in the wavenumber interval of 1000 to 1800 cm^{-1} the greatest variance was found.

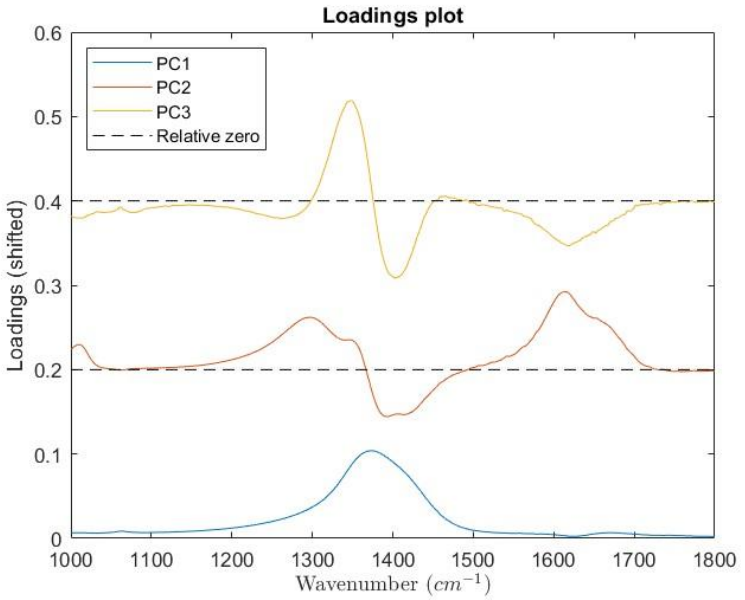

Figure 11. Loadings plot for PC_1-PC_3 where the graphs for PC_2 and PC_3 have been shifted vertically by 0.2 and 0.4 units respectively.

In *Fig. 11* it becomes clear that the most significant variances are found around 1290, 1360, 1390 and 1610 cm^{-1}.

3.2.2 Model 1 results

Upon inspection of the FTIR spectra, it was determined that Model 1 would use the transmittance at two wavenumbers, 1373 cm^{-1} and 1630 cm^{-1}, as variables. Incidentally, these wavenumbers are remarkably close to the maximums around 1360 and 1610 from the loadings plot in *Fig. 11*. This indicates that the samples exhibited significant variance around the selected wavenumbers, confirming that they were appropriately picked.

After performing LSM on the training data, linear functions for the weight fraction of K_2CO_3 and $KHCO_3$ were generated. Using these, the exact measured data was plotted against the predictions of each model in so-called parity plots (*Fig. 12*). The R^2 values were calculated in addition to the mean errors for the two parity plots, taken as the mean of the horizontal distances between the points and the perfect correlation line (*Tab. A.5*).

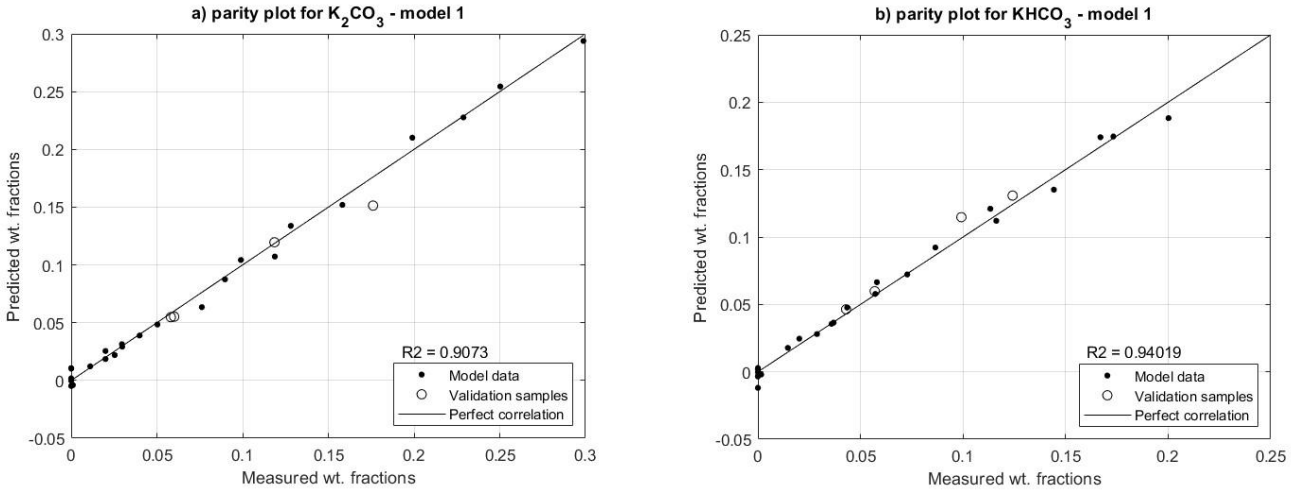

Figure 12. Parity plots for K_2CO_3 and $KHCO_3$ from model 1. Predicted model values plotted against experimental measured values.

The parity plots in *Fig. 12* plots the predicted values using model 1 against the exact values obtained from weighing in K_2CO_3 and $KHCO_3$ salts for the training set and validation set. The plots also contain a help line with a slope equal to 1, defining perfect correlation between model prediction and actual values. In both *Fig. 12a)* and *b)*, the data points are gathered about the perfect correlation lines and the distance from the points to the line on the y-axis represent the error in the prediction.

The parity plots show the ability of model 1 to predict the weight fractions of K_2CO_3 and $KHCO_3$. Looking at the R^2 values correlating to the validation samples, there is a slightly better prediction of weight fractions in the parity plot for $KHCO_3$ than for K_2CO_3. The R^2 value for K_2CO_3 might be affected by the validation sample around (0.17, 0.15) in *Fig. 12a)* that seems to deviate slightly more than the other samples. To be able to determine whether model 1 predicts weight fractions of $KHCO_3$ with greater accuracy than weight fractions of K_2CO_3, more validation samples should be included. However, the validation samples in the parity plots indicate that model 1 is able to predict the weight factions of K_2CO_3 and $KHCO_3$ with sufficient credibility.

3.2.3 Model 2 results

The linear functions created using model 2 with principal components PC_1-PC_3 were used to calculate predicted weight fractions for K_2CO_3 and $KHCO_3$. To examine the accuracy of model 2, parity plots for each function were created (*Fig. 13*). Furthermore, the R^2-values and the mean errors were calculated for the validation samples for each species.

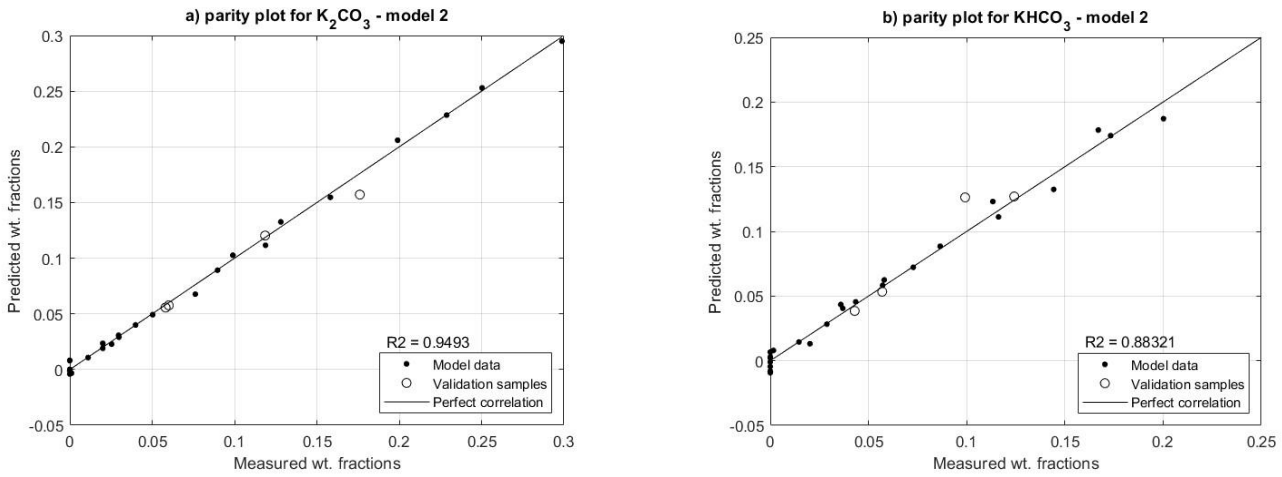

Figure 13. Parity plots for a) K_2CO_3 and b) $KHCO_3$ from model 2. Predicted model values plotted against experimental measured values.

Fig. 13 shows the training and validation data and as in *Fig. 12*, there are help lines for perfect correlation in both plots. As *Fig. 13* shows, most data points are gathered closely around the perfect correlation lines, however the *a)*-plot for K_2CO_3 displays a closer fit than the *b)*-plot for $KHCO_3$. This is also reflected in the R^2-values, where the *b)*-plot pertaining to $KHCO_3$ displays a lesser R^2-value. The parity plot in *Fig. 13b)* has a deviating sample (0.1, 0.13) which is most likely the reason for the lower R^2 value. However, model 2's predictions of K_2CO_3 and $KHCO_3$ weight fractions have a decent accuracy.

3.2.4 Model comparison

It can be concluded that both model 1 and model 2 are able to predict the weight fractions of K_2CO_3 and $KHCO_3$, as supported by the R^2 values and mean errors in *Tab. A.5*. It appears that weight fractions of K_2CO_3 were best predicted by model 2, whereas weight fractions of $KHCO_3$ were predicted better by model 1. Overall, model 1 produced more accurate predictions compared to model 2, when comparing the mean R^2 values of 0.9677 and 0.9163 respectively. This trend appears marginally when studying the mean errors in *Tab. A.5*, where model 1 had a mean error of $7.78 \cdot 10^{-3}$ and model 2's mean error was $7.96 \cdot 10^{-3}$. However, it should be noted that this is based on only four validation samples and to more firmly establish this trend, a larger validation set would be needed. In addition, both *Fig. 12a)* and *13b)* each contain a validation data point that deviate notably more than the others. Incidentally, these data points pertain to one validation sample, and removing it from the calculations yield significantly higher R^2-values of approximately 0.99. It is however hard to draw conclusions on whether to exclude this data point or not as it constitutes a quarter of the validation set.

Model 1 relies on significantly less data than model 2, as it only uses training data at two wavenumbers per sample. Model 2 on the other hand uses data from an interval of 801 wavenumbers that are recalculated to three scores per sample. This means that model 1 is less

computationally heavy compared to model 2, which is a desirable trait for a numerical model. On the other hand, this comes at the expense of the models ability to produce high fidelity data in presence of disturbances. If the absorbent contains pollutants that absorb IR radiation around 1373 cm^{-1} and 1630 cm^{-1}, it could possibly render model 1 completely inaccurate.

It should be noted that while this project utilises model 1 and 2 to evaluate the FTIR technology's feasibility, they are not necessarily the best suited for implementation. It may be that some other approach using different data analysis methods could yield more accurate predictions. This is outside the scope of this project, but could be an interesting way to further develop the method. Furthermore, to more appropriately evaluate how FTIR performs on a larger scale and in an industry scenario, it should be applied to a pilot plant. This would enable testing the technology in solvent streams, at the relevant operating temperatures, and in environments that better simulate the actual process.

By applying *Eq. 5.3* to *Eq. 5.1-5.2* and using the mean errors for K_2CO_3 and $KHCO_3$ from *Tab. A.5*, the resulting mean errors for the estimated solvent strength X and the estimated solvent loading θ-values were determined. The derivations and resulting functions can be found in *Eq. A.1* and *A.2*. The errors in X and θ derived using *Eq. 5.3* are functions of the weight fractions of K_2CO_3 and $KHCO_3$ as *Eq. 5.1-5.2* are non-linear. The resulting function surface for X and θ errors respectively for each model are illustrated in *Fig. 14*.

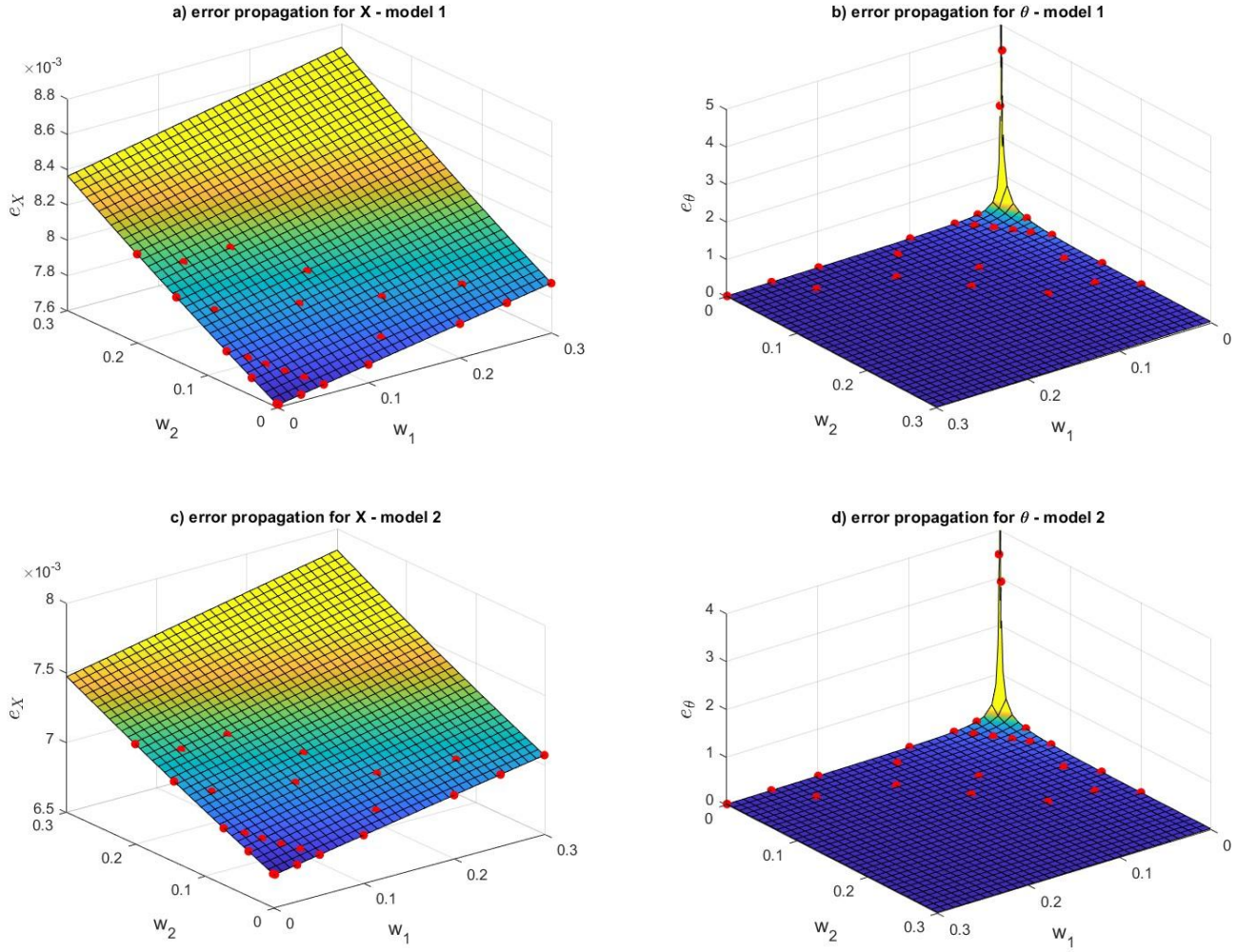

Figure 14. Error propagation plots for each model for the transformation from weight fractions to solvent strength X and solvent loading θ. The training set data is marked with red points.

As the error propagation function surfaces in *Fig. 14a)* and *c)* show, the errors in X increase with the weight fractions of K_2CO_3 and $KHCO_3$ and is in the order of 10^{-3}. However, the error propagation function surfaces in *Fig. 14b)* and *d)* display a completely different behaviour. Both function surfaces increase as the weight fractions of K_2CO_3 and $KHCO_3$ decrease, and asymptotically blows up as both weight fractions approach zero simultaneously. As *Eq. A.2* shows, the function for the θ-error indeed becomes undefined when both weight fractions equal 0. In summary, for any given set of weight fractions, the errors in X can be expected to remain close in value to the weight fraction errors. The errors in θ on the other hand are only small as long as the weight fractions are not both close to zero. In such cases, even small errors in weight fractions could create large deviances in the calculated θ-value. However, normal operation of a BECCS facility usually occurs at higher weight fractions of K_2CO_3 and $KHCO_3$. As such, the asymptotical behaviour observed in *Fig. 14b)* and *d)* is not of great concern.

3.3 Case study of field samples from Stockholm Exergi

The 10 samples provided from Stockholm Exergi were also analysed. The samples were collected at different times during a pilot plant trial run on 2023-04-03. Five of them were rich solvents and five were lean solvents. The FTIR spectra between the rich and lean solvent from the same hour is shown in *Fig. 15*.

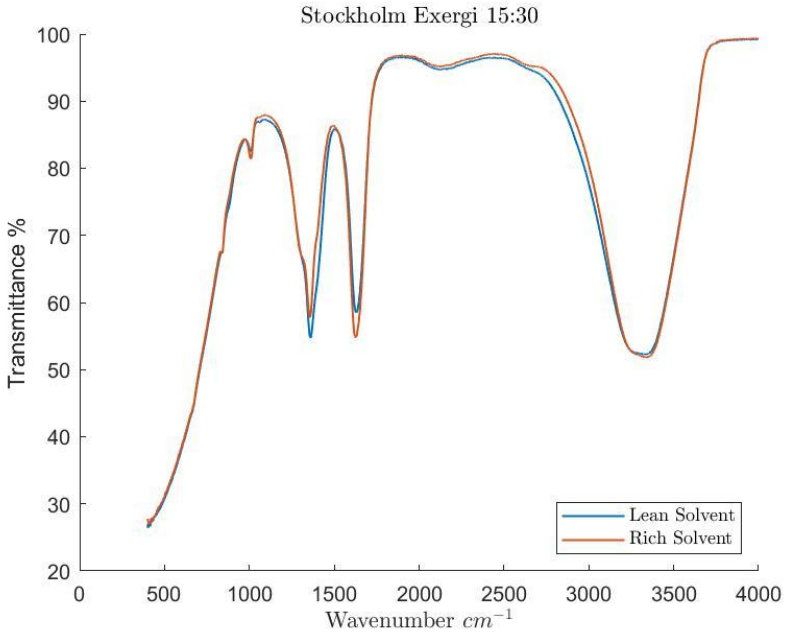

Figure 15. FTIR spectra of the rich and lean solvent provided by Stockholm Exergi from the same hour.

As the spectra above show, the expected peaks for solvents with high weight fractions of K_2CO_3 and $KHCO_3$ respectively are visible. The lean solvent displays the former peak characteristics and the rich solvent displays the latter. The lean solvent displays a higher absorbance around 1300 cm^{-1} which corresponds to a solution with lower solvent loading. The rich solvent displays higher absorbance around 1600 cm^{-1} which corresponds to a solution with higher solvent loading. This indicates that FTIR can distinguish between K_2CO_3 and $KHCO_3$ in samples collected from a real pilot plant facility. The received samples had a light green colour and a white precipitate, whereas the samples prepared in the laboratory were completely transparent and colourless. This indicates the presence of pollutants in the Stockholm Exergi samples that could disturb the measurements. However, the fact that FTIR still produced well defined spectra is a testament to the method's robustness.

To further examine the Stockholm Exergi samples, model 2 (the model based on PCA) was applied to the obtained FTIR spectra to predict weight fractions of K_2CO_3 and $KHCO_3$. The resulting predictions were used for the parity plots shown in *Fig. 16*.

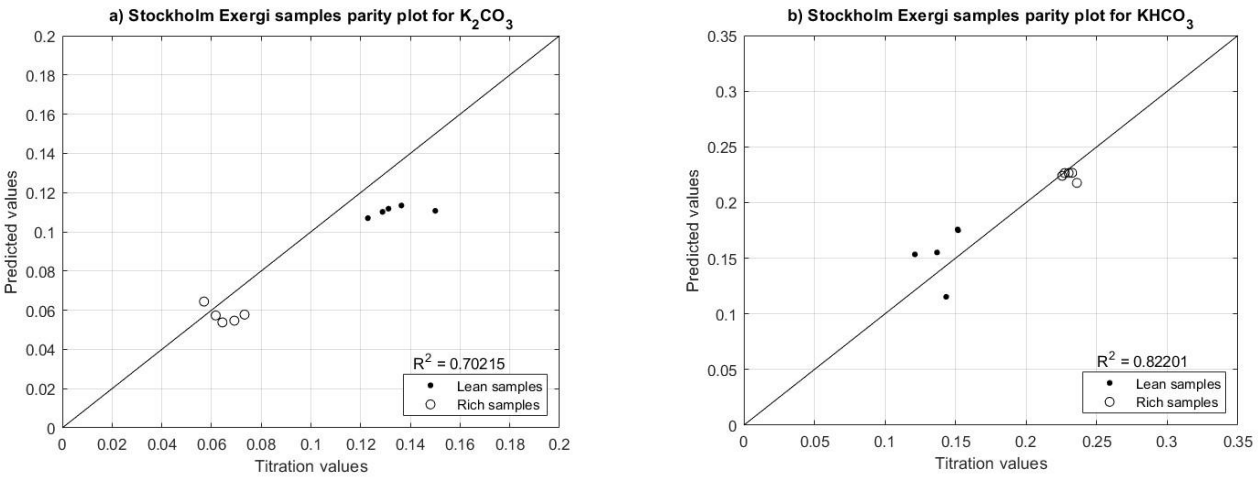

Figure 16. Parity plots for predicted weight fractions of a) K_2CO_3 and b) $KHCO_3$ from Stockholm Exergi

In *Fig. 16*, the points representing the lean and rich solvents respectively are clustered around separate areas. *Fig. 16b)* show that the rich samples have a higher weight fraction of $KHCO_3$ than the lean. As the reaction in *Eq. 3* shows, dissolved CO_2 reacts with the K_2CO_3 and water to form $KHCO_3$, meaning that the trend in *Fig. 16b)* is indeed expected. Furthermore, in *Fig. 16* it seems like the rich samples display a better fit to the perfect correlation line than the lean ones. A plausible explanation to this phenomenon is the fact that the rich samples contain more absorbing species than the lean, making it easier for FTIR to detect them. Lastly, comparing the R^2 values from *Fig. 16* to the ones in *Fig. 13*, it becomes clear that model 2 is less accurate when applied to the Stockholm Exergi samples. One notable factor that might contribute to this is that the model was created with a training set of non-polluted samples. However, as previously mentioned, the Stockholm Exergi samples were expected to contain some pollutants, judging by the difference in colour and the presence of precipitate. This could have an effect on the models performance, and one way to combat this issue might be to use a training set using samples directly from Stockholm Exergi. Additionally, the titration used to collect the reference values was conducted in a laboratory at Stockholm Exergi, which means that the accuracy of the titration has not been evaluated.

3.4 Market Overview of FTIR Probes

In this part of the report, an analysis of real-time FTIR devices will be made. Manufacturers and products that are available will be reviewed and compared. There are several manufacturers of FTIR probes that could be adapted to the purpose presented in this project.

The Swedish company ABB has several FTIR products that are adapted for different applications and has one of the world's largest portfolios when it comes to FTIR and FTNIR instruments (11). ABB offers FTIR instruments for several different applications. Many of the instruments have specifications that match the requirements for the intended use. Two of the instruments that can make real-time measurements are "*In-situ* reaction monitoring analyzer MB-Rx" and "FTPA2000_260PH". However the two instruments target different

applications (12,13). (13) The latter “FTPA2000_260PH” targets pharmaceutical manufacturing processes and uses fiber optics to make real-time measurements. However, the instrument operates in ranges that fall within the Near IR range, which falls outside the intended range for the application in this work (13). The first mentioned, “*In-situ* reaction monitoring analyzer MB-Rx”, is equipped with several probes that target different ranges of IR interval. (12). This instrument is aimed at the lab scale or pilot plant. ABB describes the application of the probe as follows “Chemical reaction in flow or batch reactor requires a fast and efficient method to measure the consumption of reactants as well as the formation of products and by-products in order to optimise an industrial process in the shortest time possible” (12) which agrees well with one of the identified the purposes that an FTIR probe must fulfil in our project.

The company Mettler Toledo (Greinfensee, Switzerland) offers FTIR probes for different types of applications. Mettler Toledo offers several FTIR probes that can be used for real-time analyses, and many of these are fitted for lab use. There are also instruments that target several applications such as the instrument "ReactIR 45P HL". This instrument is aimed both at lab use but also for pilot plants or production, which means that this could be adapted to the purpose in this report. (14)

Another company that offers high-performance measuring instruments is Bruker (Billerica, Massachusets) , who target applications within the life sciences and molecular research. The company also sells the instrument "MATRIX-MF" which uses optical fiber probes that enables *in-situ* analysis. (15,16)

Lastly, the company art photonics (Berlin, Germany) offers the product line "FlexiSpec" which are Near IR and Mid IR probes that can be used for many types of FT-NIR and FTIR spectrometers. These probes are adaptable for reaction control on lab scale, pilot plant, and fully automated process scale. (17)

An overview of the market for *in-situ* and real-time analysis using FTIR shows that the range is large and that the customization options are many. As described above, there are many different instruments from several different manufacturers that could potentially be used to do *in-situ* real-time analysis of captured CO_2 during absorption. This makes the ability to make real-time and *in-situ* FTIR measurements completely possible from a lab technical perspective.

Based on the market overview of FTIR products, a hypothesis can be made for which of the listed products could be best adapted to the BECCS application with the potassium carbonate process. The hypothesis is that Mettler Toledos product “ReactIR 45P HL” is most suitable product for the application that this work concerns. This hypothesis is drawn based on several reasons. Firstly, it is described that "ReactIR 45P HL" enables processes to be moved from lab scale to pilot plants but also to larger productions (14). Secondly, Mettler Toledo is a global company that targets several types of laboratory and process equipment. Including a number of products and sub-areas within “Automated reactors & *in-situ* analysis for chemical

process development”(18).Within this sub area, the area of use of these products is described as follows “Automated synthesis reactors and controlled laboratory reactors replace traditional round bottom flasks or jacketed lab reactors”(18). This description agrees well with the purpose of being able to obtain *in-situ*, real-times analysis well, which gives an indication that the ReactIR 45P HL would be a good instrument to meet the purpose of this project.

4. Conclusions

- FTIR is sensitive enough to distinguish between K_2CO_3 and $KHCO_3$.
- FTIR is robust enough and is not significantly affected by gaseous incineration products other than CO_2. It seems insensitive to absorbed soot, however, ammonia leaves a clear imprint on the FTIR spectra.
- Inclusion of V_2O_5 as a rate promoter does not interfere with FTIR measurements.
- Model 1 and model 2 are both able to predict the weight fractions of K_2CO_3 and $KHCO_3$ with sufficient accuracy.
- Implementation of this method in BECCS facilities would require further testing of an FTIR probe on a pilot plant scale.

5. Acknowledgements

We wish to thank our supervisor associate professor **Matthäus Bäbler** (Division of Process Technology, KTH) for the opportunity to conduct this project and for excellent guidance. We would also like to thank **Nima Mirzaei** for assistance in the laboratory and valuable discussions. Lastly we wish to thank **Love Wiklund** for valuable discussion and good collaboration.

6. References

1. IPCC. Global Warming of 1.5°C: IPCC Special Report on Impacts of Global Warming of 1.5°C above Pre-industrial Levels in Context of Strengthening Response to Climate Change, Sustainable Development, and Efforts to Eradicate Poverty [Internet]. Cambridge: Cambridge University Press; 2022 [cited 2023 Apr 19]. Available from: https://www.cambridge.org/core/books/global-warming-of-15c/D7455D42B4C820E706A03A169B1893FA
2. Wretborn S. What is Carbon Dioxide Removal – CDR - Beccs Stockholm [Internet]. [cited 2023 Apr 19]. Available from: https://beccs.se/cdr/what-is-carbon-dioxide-removal-cdr/
3. Fuss S, Canadell JG, Peters GP, Tavoni M, Andrew RM, Ciais P, et al. Betting on negative emissions. Nat Clim Change. 2014 Oct;4(10):850–3.
4. Rosa L, Sanchez DL, Mazzotti M. Assessment of carbon dioxide removal potential via BECCS in a carbon-neutral Europe. Energy Environ Sci. 2021 May 19;14(5):3086–97.
5. Gustafsson K, Sadegh-Vaziri R, Grönkvist S, Levihn F, Sundberg C. BECCS with combined heat and power: Assessing the energy penalty. Int J Greenh Gas Control. 2021 Jun;108:103248.
6. Ghosh U, Kentish S, Stevens G. Absorption of carbon dioxide into aqueous potassium carbonate promoted by boric acid. Energy Procedia. 2009 Feb 28;1:1075–81.
7. Skilton RA, Parrott AJ, George MW, Poliakoff M, Bourne RA. Real-Time Feedback Control Using Online Attenuated Total Reflection Fourier Transform Infrared (ATR FT-IR) Spectroscopy for Continuous Flow Optimization and Process Knowledge. Appl Spectrosc. 2013 Oct 1;67(10):1127–31.
8. Esbensen KH, Swarbrick B, Westad F, Whitcombe P, Anderson MJ. Multivariate Data Analysis: An Introduction to Multivariate Analysis, Process Analytical Technology and Quality by Design. 6th ed. Oslo, Norway: CAMO Software As; 2018.
9. Milella F, Mazzotti M. Estimating speciation of aqueous ammonia solutions of ammonium bicarbonate: application of least squares methods to infrared spectra. React Chem Eng. 2019 Jun 25;4(7):1284–302.
10. Palencia M. Functional transformation of Fourier-transform mid-infrared spectrum for improving spectral specificity by simple algorithm based on wavelet-like functions. J Adv Res. 2018 Nov 1;14:53–62.
11. ABB. FTIR and FT-NIR Spectrometers [Internet]. [cited 2023 Mar 20]. Available from: https://new.abb.com/products/measurement-products/analytical/ft-ir-and-ft-nir-analyzers
12. ABB. In-situ Reaction Monitoring Analyzer - MB-Rx [Internet]. Measurement Products. [cited 2023 Mar 20]. Available from: https://new.abb.com/products/measurement-products/analytical/ft-ir-and-ft-nir-analyzers/laboratory-spectrometers/mb-rx
13. ABB. FT-NIR Process Analyzer for Pharmaceutical and Life Science Industry - FTPA2000-260PH [Internet]. Measurement Products. [cited 2023 Mar 20]. Available from: https://new.abb.com/products/measurement-products/analytical/ft-ir-and-ft-nir-analyzers/process-spectrometers/ftpa2000-260ph
14. Mettler Toledo. ReactIR 45P HL Process FTIR [Internet]. [cited 2023 Mar 22]. Available from: https://www.mt.com/se/sv/home/products/L1_AutochemProducts/ftir-and-raman-spectrometers/ftir-spectrometers/reactir-45p-HL-Process-FTIR.html
15. Bruker. MATRIX-MF FT-IR Process Reaction Monitoring [Internet]. [cited 2023 Mar 24]. Available from: https://www.bruker.com/en/products-and-solutions/infrared-and-raman/ft-ir-nir-for-process-control/matrix-mf-ft-ir-reaction-monitoring.html
16. Bruker. About Bruker [Internet]. [cited 2023 Mar 24]. Available from: https://www.bruker.com/en/about.html
17. art photonics. Products [Internet]. [cited 2023 Mar 27]. Available from: https://artphotonics.com/products/
18. Mettler Toledo. Automated Reactors and In-Situ Analysis [Internet]. [cited 2023 Apr 25]. Available from: https://www.mt.com/us/en/home/products/L1_AutochemProducts.html

7. Appendices

Table A.1. Training set data. The table consists of weight fraction of K_2CO_3 and $KHCO_3$, solvent strength X, solvent loading θ and the scores t_1, t_2 and t_3.

	Wt. fraction K_2CO_3	Wt. fraction $KHCO_3$	X	θ	t_1	t_2	t_3
S1	0.2503	0	0.2503	0	1125.2	1007.9	-625.0113
S2	0.0503	0	0.0503	0	1474.4	1001.2	-607.4224
S3	0.0253	0	0.0253	0	1519.7	995.3	-613.6097
S4	0.0010	0	0.0010	0	1565.6	989.2	-621.8784
S5	0	0.2001	0.1445	1.0000	1373.1	835.4	-620.5693
S6	0	0.0728	0.0511	1.0000	1498.6	932.3	-625.3225
S7	0	0.0369	0.0257	1.0000	1530.3	959.7	-624.3351
S8	0	0.0016	0.0011	1.0000	1565.7	987.9	-622.3308
S9	0.1582	0.0580	0.2008	0.2021	1227.4	951.4	-605.7712
S10	0.0399	0.0146	0.0502	0.2013	1477.6	986.7	-611.3723
S11	0.0762	0.1670	0.1988	0.6020	1271.4	848.4	-607.4317
S12	0.0200	0.0435	0.0506	0.6002	1488.0	957.5	-618.7673
S13	0.2288	0.0359	0.2555	0.0977	1119.5	967.8	-616.8921
S14	0.1281	0.0202	0.1427	0.0983	1311.7	993.7	-601.8700
S15	0.1188	0.1133	0.2021	0.3970	1245.5	898.0	-605.0076
S16	0.0897	0.0865	0.1522	0.3996	1317.7	926.9	-604.4272
S17	0.0296	0.0288	0.0499	0.4018	1481.7	973.9	-613.9061
S18	0.0298	0.1733	0.1554	0.8004	1347.1	848.6	-615.9554
S19	0.0200	0.1162	0.1028	0.8007	1417.5	901.5	-618.4305
S20	0.0111	0.0572	0.0512	0.7804	1491.8	945.4	-622.1284
S21	0.2988	0	0.2988	0	1051.2	999.8	-641.7563
S22	0.1990	0	0.1990	0	1206.3	1014.1	-608.6490
S23	0.0990	0	0.0990	0	1384.1	1010.9	-600.7806
S24	0	0.1443	0.1028	1.0000	1426.6	881.6	-623.0079

Table A.2. Validations set data.

	Wt. fraction K_2CO_3	Wt. fraction $KHCO_3$	X	Theta
V1	0.1186	0,043	0.15	0.2002
V2	0.0601	0,1242	0.15	0.5879
V3	0.1761	0.0992	0.25	0.28
V4	0.0581	0.057	0.099	0.4035
SE-L1	0.1107	0.1534	0.2241	0.4889
SE-L2	0.1102	0.1153	0.1947	0.4194
SE-L3	0.1118	0.1750	0.2419	0.5194
SE-L4	0.1134	0.1758	0.2442	0.5170
SE-L5	0.1070	0.1551	0.2216	0.5003
SE-R1	0.0644	0.2176	0.2254	0.6998
SE-R2	0.0538	0.2266	0.2212	0.7440
SE-R3	0.0547	0.2267	0.2222	0.7411
SE-R4	0.0578	0.2240	0.2234	0.7280
SE-R5	0.0573	0.2265	0.2248	0.7317
Polluted abs.liq.	0.1619	0	0.1619	0
Clean abs.liq.	0.1619	0	0.1619	0
Polluted NH_4Cl	0.1498	0.1001	0.2238	0.3155

Table A.5. Polluted samples containing vanadium pentoxide.

Wt. fraction K_2CO_3	Wt. fraction $KHCO_3$	Theta	X	Wt. fraction V_2O_5
0.2503	0	0	0.2503	0
0.2444	0	0	0.2443	0.0240
0.2378	0	0	0.2378	0.0501
0.1032	0.1498	0.5005	0.2136	0
0.1006	0.1460	0.5005	0.2081	0.0250

*Table A.4. Infrared band assignments. The symbols **ν**, ν_a and δ corresponds to symmetric stretching, asymmetric stretching and the bending mode respectively. (9)*

Species	Band position [cm^{-1}]	Assignment
H_2O	1640	$\delta(H_2O)$[20]
$CO_2(aq)$	2343	$\nu_a(CO_2)$[20]
$NH_3(aq)$	1111	$\delta(NH_3)$[20]
NH_4^+	1458	$\delta(-NH)$[20]
CO_3^{2-}	1395	$\nu_a(-CO)$[21]
NH_2COO^-	1120	$\nu(-CN)$[11,22,23]
	1413	$\nu(-CN)$[11,24]
	1545	$\delta(-N-H)$[11,22]
HCO_3^- (ref. 21)	1005	$\nu_a(-C-OH)$
	1300	$\delta(-C-OH)$
	1365	$\nu(-C-O)$
	1650	$\nu_a(-C-O)$

Table A.5. R^2-values and mean errors from each parity plot

Function	**R^2**	**Mean error $\times 10^{-3}$**
Mod.1 training set - CO_3	0.9951	4.7780
Mod. 2 training set - CO_3	0.9977	3.2404
Mod. 1 training set - HCO_3	0.9924	4.1122
Mod. 2 training set - HCO_3	0.9893	5.0694
Mod. 1 validation set - CO_3	0.9951	8.4883
Mod. 2 validation set - CO_3	0.9493	6.4099
Mod. 1 validation set - HCO_3	0.9402	7.0687
Mod. 2 validation set - HCO_3	0.8832	9.5024
Model 1 validation set mean	0.9677	7.7785
Model 2 validation set mean	0.9163	7.9562
Sthlm Exergi samples - CO_3	0.7021	16.876
Sthlm Exergi samples - HCO_3	0.8220	15.625

Equation A.1

$$\frac{\partial X}{\partial w_1} = \frac{\partial}{\partial w_1}\left(\frac{2w_1M_2+w_2M_1}{2(1-w_2)M_2+w_2(M_1+M_3)}\right) = \frac{2M_2}{w_2(M_1+M_3-2M_2)+2M_2}$$

$$\frac{\partial X}{\partial w_2} = \frac{\partial}{\partial w_2}\left(\frac{2w_1M_2+w_2M_1}{2(1-w_2)M_2+w_2(M_1+M_3)}\right) = \frac{M_1(w_2(M_1+M_3-2M_2)+2M_2)-(2w_1M_2+w_2M_1)(M_1+M_3-2M_2)}{(w_2(M_1+M_3-2M_2)+2M_2)^2} = \frac{2M_1M_2-2w_1M_2(M_1+M_3-2M_2)}{(w_2(M_1+M_3-2M_2)+2M_2)^2}$$

$$e_X = \left|\frac{\partial X}{\partial w_1}\right| e_{w1} + \left|\frac{\partial X}{\partial w_2}\right| e_{w2} = \left|\frac{2M_2}{w_2(M_1+M_3-2M_2)+2M_2}\right| e_{w1} + \left|\frac{2M_1M_2-2w_1M_2(M_1+M_3-2M_2)}{(w_2(M_1+M_3-2M_2)+2M_2)^2}\right| e_{w2}$$

Equation A.2

$$\frac{\partial \theta}{\partial w_1} = \frac{\partial}{\partial w_1}\left(\frac{w_2}{2(M_2/M_1)w_1+w_2}\right) = \frac{-2(M_2/M_1)w_2}{(2(M_2/M_1)w_1+w_2)^2}$$

$$\frac{\partial \theta}{\partial w_2} = \frac{\partial}{\partial w_2}\left(\frac{w_2}{2(M_2/M_1)w_1+w_2}\right) = \frac{2(M_2/M_1)w_1+w_2-w_2}{(2(M_2/M_1)w_1+w_2)^2} = \frac{2(M_2/M_1)w_1}{(2(M_2/M_1)w_1+w_2)^2}$$

$$e_\theta = \left|\frac{\partial \theta}{\partial w_1}\right| e_{w1} + \left|\frac{\partial \theta}{\partial w_2}\right| e_{w2} = \left|\frac{-2(M_2/M_1)w_2}{(2(M_2/M_1)w_1+w_2)^2}\right| e_{w1} + \left|\frac{2(M_2/M_1)w_1}{(2(M_2/M_1)w_1+w_2)^2}\right| e_{w2}$$

Attachment 1

Mimicking loaded potassium carbonate solvents

Matthaus U. Babler[1],*

[1] *Department of Chemical Engineering, KTH Royal Institute of Technology, SE-10044 Stockholm, Sweden*

(Dated: February 21, 2023)

A. Characteristics of carbonate solvents

Carbon dioxide injected into an aqueous solution of potassium carbonate reacts with the solvent components according to:

$$\underset{\mathbf{1}}{K_2CO_3} + CO_2 + \underset{\mathbf{3}}{H_2O} \rightleftharpoons \underset{\mathbf{2}}{2\,KHCO_3} \tag{1}$$

To simplify the notation, let us denote the carbonate by **1**, the bicarbonate by **2**, and water by **3**.

The absorption solvent is typically described by two quantities: (1) the solvent strength X, defined as the weight percent of K_2CO_3 in the native solvent (the solvent that has not yet absorbed any CO_2), and (2) the solvent loading θ, defined is the moles of CO_2 taken up by the solvent divided by the moles of K_2CO_3 in the native solvent. The solvent strength is often reported as w% of K_2CO_3-*equivalents*. Adopting this terminology, we can expresss the solvent strength X as:

$$X = \text{w\% equiv. } K_2CO_3 \text{ (solvent strength)}, \tag{2}$$

while the solvent loading can be expressed as:

$$\theta = \frac{\text{(Moles } CO_2 \text{ absorbed)}}{\text{(Moles } K_2CO_3\text{-equivalents)}} \tag{3}$$

The denominator of Eq. (3) is often written in terms of c_{K_2}, i.e. the concentration of (hypothetical) $K_2{}^{2+}$ units. Fig. 1 illustrates the characterisation of the solvent in the X-θ-plane. An absorption solvent that has taken up some CO_2 is described by a point in this plane.

This note aims at establishing the formulas to calculate the amounts of pure K_2CO_3 and pure $KHCO_3$ that have to be dissolved to *mimic* an absorption solvent with strength X and loading θ.

TABLE I: Molecular weights

Substance		M_i (g/mol)
1	K_2CO_3	138.2
2	$KHCO_3$	100.1
3	H_2O	18.0

* babler@kth.se

B. Mimicking a loaded K_2CO_3 solvent

To proceed we notice that the solvent loading as defined in Eq. (3) can also be interpreted as the conversion of Reaction 1. Hence, the number of moles of K_2CO_3, $KHCO_3$, and H_2O in a solvent with loading θ read as:

$$n_1 = n_{10}(1-\theta) \tag{4a}$$
$$n_2 = 2\,\theta n_{10} \tag{4b}$$
$$n_3 = n_{30} - n_{10}\theta \tag{4c}$$

where n_{10} and n_{30} are the number of moles of K_2CO_3 and H_2O in the native solvent. Using the solvent strength X the latter quantities read as:

$$n_{10} = \frac{m_s X}{M_1}, \qquad n_{30} = \frac{m_s(1-X)}{M_3} \tag{5}$$

where m_s is the mass of the solvent and M_i is the molecular weight of component i. Notice that the relations in Eq. (4) are in agreement with the commonly used formula that relates solvent loading to the concentration of carbonates and bicarbonates, i.e.

$$\theta = \frac{[HCO_3{}^-]}{2[CO_3{}^{-2}] + [HCO_3{}^-]} = \frac{n_2}{2n_1 + n_2} \tag{6}$$

The aim is to find the weight fraction of K_2CO_3 and $KHCO_3$ that make up the solvent with strength X and loading θ. Expressed with number of moles and molecular weights, the weight fraction of K_2CO_3 and $KHCO_3$ read as:

$$w_1 = \frac{n_1 M_1}{n_1 M_1 + n_2 M_2 + n_3 M_3} \tag{7a}$$
$$w_2 = \frac{n_2 M_2}{n_1 M_1 + n_2 M_2 + n_3 M_3} \tag{7b}$$
$$w_3 = 1 - w_1 - w_2 \tag{7c}$$

Substituting n_i for Eq. (4) and using the relations (5) we obtain:

$$w_1 = \frac{1-\theta}{1 + b\theta + (1-X)/X} \tag{8a}$$
$$w_2 = \frac{2\theta\, M_2/M_1}{1 + b\theta + (1-X)/X} \tag{8b}$$
$$w_3 = 1 - w_1 - w_2 \tag{8c}$$

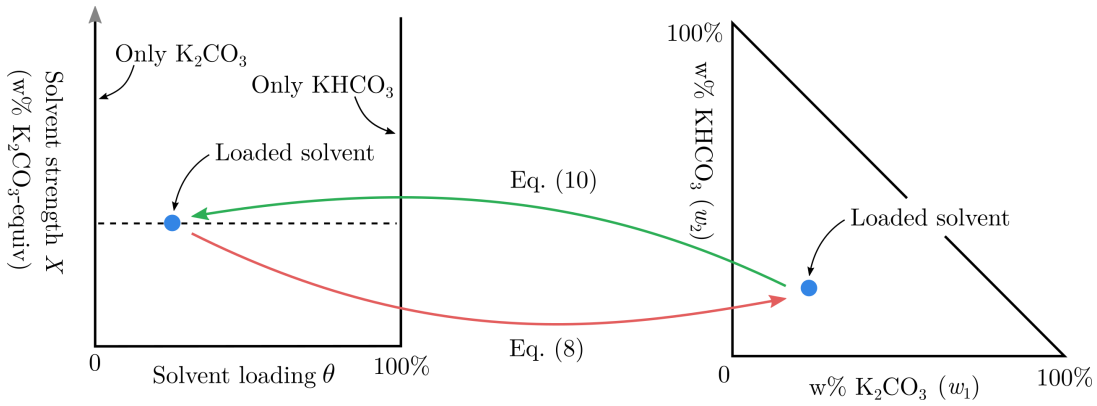

FIG. 1: A loaded solvent is characterized by the solvent strength X and the solvent loading θ. Eq. (8) allows for calculating the weight fractions of K_2CO_3 (w_1) and $KHCO_3$ (w_2) to weigh in to mimic the solvent. The reverse calculation, i.e. obtaining the strength and the loading from w_1 and w_2 is given by Eq. (10).

where

$$b = \frac{2M_2}{M_1} - \frac{M_3}{M_1} - 1 \approx 0.318 \tag{9}$$

(the numerical value has been calculated using the molecular weights given in Tab. I).

It is also interesting to consider the opposite case, i.e. given a solution containing K_2CO_3 and $KHCO_3$ at a weight fraction w_1 and w_2, respectively, the solvent strength and the solvent loading equate as:

$$X = \frac{2w_1M_2 + w_2M_1}{2(1-w_2)M_2 + w_2(M_1+M_3)} \tag{10a}$$

$$\theta = \frac{w_2}{2(M_2/M_1)w_1 + w_2} \tag{10b}$$

TABLE II: Sample calculations

Solvent	Weight fractions w_1 and w_2	
	Eq. (8) with $b = 0.318$	Eq. (8) with $\hat{b} = 0.449$
X=20%, θ=70%	w_1=0.057 w_2=0.194	$\hat{w}_1$=0.056 $\hat{w}_2$=0.191
X=30%, θ=85%	w_1=0.042 w_2=0.342	$\hat{w}_1$=0.040 $\hat{w}_2$=0.331

Remark. It is worthwhile to investigate the effect of water in Reaction (1) on the weight fractions w_1 and w_2. To this aim the derivation was repeated where, instead of Eq. (4), a *simplified mole balance* was used where water is preserved:

$$n_1 = n_{10}(1-\theta), \quad n_2 = 2\,\theta n_{10}, \quad n_3 = n_{30}. \tag{11}$$

Repeating the derivation with Eq. (11) instead of Eq. (4) results in the same expressions as in Eq. (8), with the parameter b replaced by $\hat{b} = 2M_2/M_1 - 1 \approx 0.449$, which is around 40% larger than the original value of b. Accounting for water is particularly important for solvents with heigh loadings, as the sample calculations in Tab. II show.